


 Cite this: *RSC Adv.*, 2025, **15**, 35728

# Preparation of a nanoporous CoFe<sub>2</sub>O<sub>4</sub>/CoMoO<sub>4</sub> composite electrode material and a study on its performance in water electrolysis

 Haorui Liu,<sup>bc</sup> Qi Zhou<sup>\*ab</sup> and Dedong Duan<sup>b</sup>

In this study, a CoFe<sub>2</sub>O<sub>4</sub>/CoMoO<sub>4</sub> composite electrode material with a spinel structure (CoFe<sub>2</sub>O<sub>4</sub>) and a scheelite structure (CoMoO<sub>4</sub>) was prepared by a hydrothermal method. The rich valence states and its unique morphological and structural advantages made the CoFe<sub>2</sub>O<sub>4</sub>/CoMoO<sub>4</sub> composite electrode material play a more effective synergistic catalytic role. Results of the electrochemical characterization showed that CoMoO<sub>4</sub> was attached to the CoFe<sub>2</sub>O<sub>4</sub> skeleton structure in the composite electrode in a sheet form. At a current density of 50 mA cm<sup>-2</sup>, the hydrogen evolution overpotential was 193 mV and the respective Tafel slope was 100.44 mV dec<sup>-1</sup>, while the oxygen evolution overpotential was 319 mV and the corresponding Tafel slope was 70.47 mV dec<sup>-1</sup>. At the same time, the overall water decomposition voltage was 1.55 V at a current density of 10 mA cm<sup>-2</sup>, and the voltage changed only 11 mV for a 12 h continuous electrolysis, which suggested a good electrocatalytic water decomposition performance.

 Received 18th July 2025  
 Accepted 3rd September 2025

DOI: 10.1039/d5ra05179g

[rsc.li/rsc-advances](http://rsc.li/rsc-advances)

## 1 Introduction

The development of safe, clean and sustainable energy sources is a major topic and technological challenge of the 21st century.<sup>1–5</sup> As a green energy source with high energy density, H<sub>2</sub> is widely regarded as the most promising clean and renewable energy source. Electrolysis of water for hydrogen production is an extremely attractive solution, which can produce hydrogen sustainably.<sup>6,7</sup> Because the overpotential loss caused by the oxygen evolution reaction (OER) is usually much greater than the potential loss caused by the hydrogen evolution reaction (HER), the OER is often regarded as the bottleneck of water decomposition.<sup>8–10</sup> Although precious metal catalysts such as Pt and RuO<sub>2</sub> have high catalytic activity, they are expensive and their reserves are limited, making it difficult to achieve large-scale application. In recent years, transition metal alloys,<sup>11,12</sup> oxides,<sup>13,14</sup> sulfides<sup>15,16</sup> and phosphates<sup>17,18</sup> have become hot topics in the field of electrocatalysis. Transition metal oxides are attractive alternatives to noble metal catalysts due to their low cost and high redox activity.

The development of non-precious metal oxide-based catalysts in alkaline solutions has become one of the most active

research areas in chemistry and materials science. Du *et al.*<sup>19</sup> designed NiCo<sub>2</sub>O<sub>4</sub> nanowires as the precursors with NiMoO<sub>4</sub> nanosheets compounded on the surface. The flower-like NiCo<sub>2</sub>O<sub>4</sub>@NiMoO<sub>4</sub> core-shell hybrid nanostructures were prepared by hydrothermal calcination. The OER overpotential of the composites was 250 mV at a current density of 10 mA cm<sup>-2</sup>. When applied to integral water decomposition, the decomposition voltage was 1.55 V at a current density of 10 mA cm<sup>-2</sup>. Zhang *et al.*<sup>20</sup> reported a novel NiMoO<sub>4-x</sub>/MoO<sub>2</sub> hybrid electrocatalyst with atomically coupled nanointerfaces and a large number of Mo<sup>5+</sup> ions. The NiMoO<sub>4-x</sub>/MoO<sub>2</sub> electrocatalyst showed excellent electrocatalytic performance for both the HER and OER in alkaline media. The Tafel slopes were 31 mV dec<sup>-1</sup> and 69 mV dec<sup>-1</sup>, and the overpotential of the HER and OER at a current density of 10 mA cm<sup>-2</sup> were 41 mV and 233 mV, respectively. It was used as a bifunctional electrode material for integral water decomposition and achieved a current density of 10 mA cm<sup>-2</sup> at a voltage of only 1.56 V.

In order to further improve the catalytic activity and stability of polymetallic oxide nanoporous electrode materials, a composite functional material was synthesized in this study. The flake-like CoMoO<sub>4</sub> was hydrothermally synthesized on a CoFe<sub>2</sub>O<sub>4</sub> spinel skeleton, forming a composite with synergistic catalytic effects for efficient overall water splitting. The composite electrode exhibited a high catalytic activity and durable stability for the electrochemical reactions of OER and HER. In this study, the electrocatalytic water decomposition performance of transition metal oxides and their composites was also tested. The relationship between phase composition, microstructure and electrocatalytic performance was studied,

<sup>a</sup>State Key Laboratory of Advanced Processing and Recycling of Non-ferrous Metals, Lanzhou University of Technology, Lanzhou, 730050, Gansu, China. E-mail: zhouxq301@sina.com

<sup>b</sup>School of Materials Science and Engineering, Lanzhou University of Technology, Lanzhou, 730050, Gansu, China

<sup>c</sup>School of Materials Engineering, Longdong University, Qingyang 745000, Gansu, China



which provided a reference for the preparation of transition metal oxides and their composites in the field of electrocatalytic water decomposition.

## 2 Experimental

### 2.1 Preparation of the electrocatalysts

The precursor alloy ingots with theoretical atomic ratios of  $\text{Co}_{1.7}\text{Fe}_{3.3}\text{Al}_{9.5}$  and  $\text{Co}_{2.5}\text{Mo}_{2.5}\text{Al}_{9.5}$  were prepared by arc-melting the metal particles of cobalt (Co), iron (Fe), molybdenum (Mo) and aluminium (Al) with purity higher than 99.9%. After removing the oxide skin of the alloy ingots, the alloy strips were rapidly solidified in a vacuum strip machine under an argon atmosphere (the pressure of the quartz tube of the strip machine was 0.12 MPa, and the speed of the copper roller was  $25 \text{ r s}^{-1}$ ), and subsequently, precursor alloy strips with a width of about 3–5 mm and a thickness of about 30–40  $\mu\text{m}$  were obtained. The nanoporous Co–Fe and Co–Mo alloys were obtained by chemical dealloying. The corrosion of the  $\text{Co}_{2.5}\text{Mo}_{2.5}\text{Al}_{9.5}$  alloy thin strip was carried out in a  $1 \text{ mol L}^{-1}$  KOH solution at  $25 \text{ }^\circ\text{C}$  for 24 h, while the corrosion of  $\text{Co}_{1.7}\text{Fe}_{3.3}\text{Al}_{9.5}$  was carried out in a  $6 \text{ mol L}^{-1}$  KOH solution at  $65 \text{ }^\circ\text{C}$  for 12 h. The dealloyed samples were thoroughly rinsed with deionized water and anhydrous ethanol until a neutral pH was achieved, followed by drying in a 563 vacuum oven at  $60 \text{ }^\circ\text{C}$  for 6 h. The dried samples were then transferred to a porcelain boat and placed in a heat treatment furnace, with the temperature increased at a rate of  $1 \text{ }^\circ\text{C min}^{-1}$ . The samples were heated to  $350 \text{ }^\circ\text{C}$  and maintained at this temperature for 2 h. Finally, nanoporous  $\text{CoFe}_2\text{O}_4$  and  $\text{CoMoO}_4$  were obtained after cooling to room temperature.

Preparation of the  $\text{CoFe}_2\text{O}_4/\text{CoMoO}_4$  composite electrode: A mixture of  $0.01 \text{ mol L}^{-1}$   $\text{Co}(\text{NO}_3)_2$ ,  $0.01 \text{ mol L}^{-1}$   $\text{Na}_2\text{MoO}_4$  and  $0.1 \text{ mol L}^{-1}$  urea was prepared for ultrasonic treatment. 30 mg of  $\text{CoFe}_2\text{O}_4$  was added to this mixture and reacted at  $150 \text{ }^\circ\text{C}$  for 8 h. Then, the obtained product was dried in a vacuum drying oven at  $60 \text{ }^\circ\text{C}$  for 6 h. The dried powder was placed in a porcelain boat and kept at  $400 \text{ }^\circ\text{C}$  in a heat treatment furnace for 2 h. After cooling to room temperature, the  $\text{CoFe}_2\text{O}_4/\text{CoMoO}_4$  composite electrode material was obtained.

Preparation of  $\text{CoMoO}_4$  on nickel foam: The nickel foam was first pretreated with  $3 \text{ mol L}^{-1}$  HCl and anhydrous ethanol for 10 minutes by sequential ultrasonic cleaning to remove surface impurities and oxide scales, respectively. Then, it was transferred to a vacuum drying oven and dried at  $60 \text{ }^\circ\text{C}$  for 6 hours.  $\text{CoMoO}_4$  was then synthesized *via* a hydrothermal method, using the same solution preparation and experimental conditions as those employed for the preparation of the  $\text{CoFe}_2\text{O}_4/\text{CoMoO}_4$  composite electrode.

20 mg of the porous material obtained after drying was taken as the active material and mixed evenly with acetylene black, conductive graphite and polytetrafluoron according to the mass percentage of 80 : 7.5 : 7.5 : 5. Appropriate amount of anhydrous ethanol was added to this paste, coated on pre-treated nickel foam with an area of  $1 \text{ cm}^2$ , and pressed into sheets after vacuum drying at  $60 \text{ }^\circ\text{C}$  for 6 h. A three-electrode system was selected for the electrocatalytic test. The auxiliary electrode was a  $15 \text{ mm} \times 10 \text{ mm}$  platinum sheet, the reference electrode was

saturated with calomel electrode, the working electrode was a foam nickel collector loaded with the active substances, and the electrolyte was a  $1 \text{ mol L}^{-1}$  KOH solution.  $\text{N}_2$  was permeated throughout the electrocatalytic test.

### 2.2 Electrochemical measurements

A standard three-electrode cell system was employed, using the as-prepared sample as the working electrode, a  $15 \text{ mm} \times 15 \text{ mm}$  Pt sheet as the counter electrode, and a saturated calomel electrode (SCE) as the reference electrode. The electrolyte was a  $1 \text{ mol L}^{-1}$  KOH solution. Throughout the electrochemical measurements, the electrolyte was continuously purged with  $\text{N}_2$  to maintain a saturated environment. Prior to LSV testing, the prepared electrode was electrochemically activated by performing 30 cycles at a fast scan rate of  $20 \text{ mV s}^{-1}$  until the curve was stabilized. Then LSV measurements were conducted at  $5 \text{ mV s}^{-1}$ . For the HER and OER LSV test results, 80% IR compensation was applied; for the overall water splitting test results, IR compensation was not performed.

## 3 Results and discussion

Fig. 1 shows the XRD patterns of the  $\text{Co}_{1.7}\text{Fe}_{3.3}\text{Al}_{9.5}$  and  $\text{Co}_{2.5}\text{Mo}_{2.5}\text{Al}_{9.5}$  precursor alloys before and after strip dealloying and after oxidation. As can be seen from Fig. 1(a), the  $\text{Co}_{1.7}\text{Fe}_{3.3}\text{Al}_{9.5}$  alloy is composed of two phases, Al (PDF#89-2769) and  $\text{Co}_2\text{Al}_9$  (PDF#65-6460). No corresponding peak lines of Fe and Fe-containing phases are observed in the figure, which is due to the existence of a face-centered cubic structure of Co and Fe at the same time, resulting in a solid solution between them. After dealloying, two phases, namely, Co–Fe and  $\text{Fe}_3\text{O}_4$  (PDF#88-0315) are obtained. Due to the formation of the solid solution between Co and Fe, compared with the standard Fe (PDF#85-1410), the peak position here is shifted to a higher angle by  $0.43^\circ$ . Some amount of Fe is easily oxidized to  $\text{Fe}_3\text{O}_4$  in the hot alkali environment of dealloying. So, there is a peak of  $\text{Fe}_3\text{O}_4$ . As can be seen from Fig. 1(b), the  $\text{Co}_{2.5}\text{Mo}_{2.5}\text{Al}_{9.5}$  alloy is composed of two phases, Al (PDF#89-2769) and  $\text{Al}_{12}\text{Mo}$  (PDF#29-0052). No Co is detected in the XRD pattern, which is also caused by the formation of a solid solution between Co and Mo. Compared with the standard Co (PDF#89-7093), the overall diffraction peak of the Co–Mo alloy obtained after dealloying of  $\text{Co}_{2.5}\text{Mo}_{2.5}\text{Al}_{9.5}$  is shifted to a lower angle by  $0.74^\circ$  as the atomic radius of Mo is greater than that of Co after the formation of the solid solution between Co and Mo, resulting in the lattice distortion of Co. At the same time, the half-peak width of the diffraction peak becomes significantly wider after dealloying, indicating that the crystallinity of the Co–Mo alloy obtained after dealloying is low. Comparing XRD patterns after dealloying, it is found that no Al phase is detected after dealloying of the two precursor alloys, indicating that the dealloying is basically complete. Fig. 1(c) shows the phases of the  $\text{CoFe}_2\text{O}_4$  and  $\text{CoMoO}_4$  bimetallic oxides obtained by oxidation after dealloying. It can be seen from the figure that pure  $\text{CoFe}_2\text{O}_4$  (PDF#79-1744) and  $\text{CoMoO}_4$  (PDF#21-0868) are obtained after oxidation.



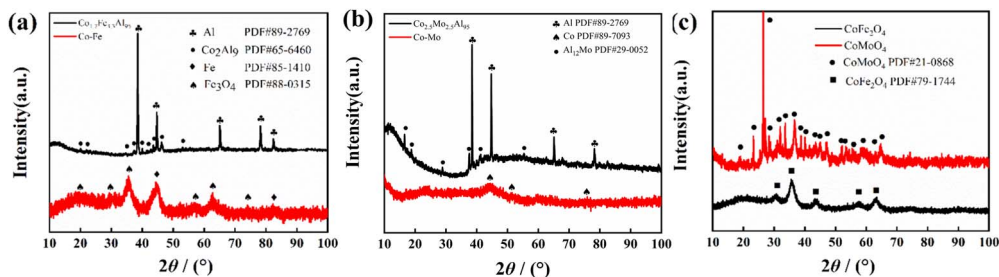


Fig. 1 XRD patterns of the precursor alloys (a)  $\text{Co}_{1.7}\text{Fe}_{3.3}\text{Al}_{95}$  and (b)  $\text{Co}_{2.5}\text{Mo}_{2.5}\text{Al}_{95}$  after dealloying and after oxidation (c).

Fig. 2 shows the SEM images of the precursor alloys after dealloying and oxidation. According to the SEM image of  $\text{Co}_{1.7}\text{Fe}_{3.3}\text{Al}_{95}$  after dealloying (Fig. 2(a)), it can be seen that a small skeleton structure of 100 nm grows on a large skeleton structure, forming a unique “attachment” structure. It is worth noting that small mesoporous structures are distributed on the surface of both large and small scaffolds. This kind of “dependent” structure loaded with mesoporous structures can provide a broad active surface area in electrochemical processes and more active sites for electrocatalytic processes. Fig. 2(b) shows  $\text{CoFe}_2\text{O}_4$  obtained after oxidation of  $\text{Co}_{1.7}\text{Fe}_{3.3}$ . Compared with the structure before oxidation, the small skeleton structure becomes rough, while the large skeleton structure supporting the small skeleton remains intact. It can be seen from Fig. 2(c) that the skeleton structure of the Co–Mo alloy after the corrosion of  $\text{Co}_{2.5}\text{Mo}_{2.5}\text{Al}_{95}$  by KOH solution presents an “island” structure connected by ligaments. This is because the

$\text{Co}_{2.5}\text{Mo}_{2.5}\text{Al}_{95}$  alloy is composed of two phases: Al and  $\text{Al}_{12}\text{Mo}$ . Al, as an active phase, preferentially reacts at the solid/liquid interface to form a large pore structure, and then, the corrosive liquid enters the deep structure to react with Al atoms in the  $\text{Al}_{12}\text{Mo}$  phase. At the same time, under the unique “pinning” action of the Mo element,<sup>21</sup> the corrosion liquid is able to react with the Al atoms in the  $\text{Al}_{12}\text{Mo}$  phase, forming an “island” structure with ligamentous connections. Fig. 2(d) shows that the ligament structure of the Co–Mo alloy still exists after oxidation, but the former “island” structure disappears and changes into a smaller skeleton structure, and a secondary ligament structure with a size of about 10–20 nm grows on the ligament structure. The evolution of this structure is due to the fact that after the Co–Mo alloy skeleton structure is oxidized, the introduced oxygen atoms cause the skeleton structure to be rough and the volume to expand, and the original “island” structure is completely transformed into a ligament-like

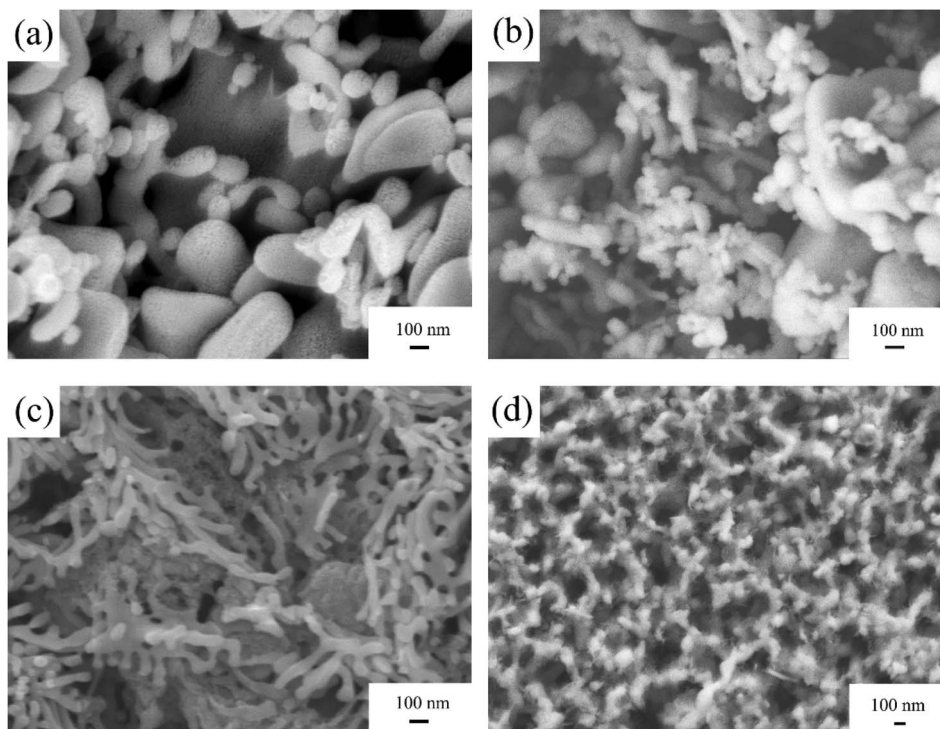


Fig. 2 SEM images of the precursor alloys after dealloying and oxidation: (a)  $\text{Co}_{1.7}\text{Fe}_{3.3}$ ; (b)  $\text{CoFe}_2\text{O}_4$ ; (c)  $\text{Co}_{2.5}\text{Mo}_{2.5}$ ; and (d)  $\text{CoMoO}_4$ .



structure, which is beneficial to the electrode material to provide more abundant reaction sites during the catalytic process.

Fig. 3(a) shows the XRD patterns of  $\text{CoMoO}_4$  synthesized by the hydrothermal method on the nickel foam (NF) matrix. As can be seen from the figure, the peak position of  $\text{CoMoO}_4$  (PDF#21-0868) is clearly visible, indicating that simple  $\text{CoMoO}_4$  samples can be synthesized by this method. Fig. 3(b) shows the XRD patterns of the  $\text{CoFe}_2\text{O}_4/\text{CoMoO}_4$  composite. It can be seen from the figure that the phase structure of the  $\text{CoFe}_2\text{O}_4$  matrix (PDF#79-1744) did not change after the introduction of  $\text{CoMoO}_4$  composite, indicating that two oxides with different phase structures were successfully prepared in this experiment.

Fig. 4 shows the SEM image of the  $\text{CoFe}_2\text{O}_4/\text{CoMoO}_4$  composite electrode material. It can be seen from the figure that  $\text{CoMoO}_4$  grows vertically on the surface of the  $\text{CoFe}_2\text{O}_4$  skeleton in the form of sheets and folds *in situ*. This heterostructure with good compatibility can not only exert a synergistic effect of the composite materials but also increase the active surface area of the material, which is conducive to more abundant  $\text{H}^+$  and  $\text{OH}^-$  adsorption and desorption, improving the electrocatalytic performance of the electrode material. In addition, the  $\text{CoMoO}_4$  and  $\text{CoFe}_2\text{O}_4$  structures show great structural compatibility. The vertically grown  $\text{CoMoO}_4$  does not extensively cover the abundant structures on the  $\text{CoFe}_2\text{O}_4$  matrix, thus preserving and

taking full advantage of its high specific surface area. The combination of the two structures will further increase the active sites for the electrochemical reaction and offer the structural advantages of both in the electrocatalytic reaction. Therefore, the  $\text{CoFe}_2\text{O}_4$  matrix plays an important role in the composite material, providing support strength for the composite electrode material, and  $\text{CoMoO}_4$  prepared by the hydrothermal method grows uniformly on the surface of the matrix. Both of them play important roles in the catalytic performance of the composite material due to their unique structural advantages.

In order to further study the composition of the  $\text{CoFe}_2\text{O}_4/\text{CoMoO}_4$  composite electrode material and the distribution of each element, EDS surface scanning analysis was performed, as shown in Fig. 5. The EDS mapping shows a spatially uniform distribution of all elements (Co, Fe, Mo, O) without clear phase boundaries. This suggests that  $\text{CoMoO}_4$  grows uniformly over the  $\text{CoFe}_2\text{O}_4$  skeleton, thereby confirming the good compatibility between the two phases. It is worth noting that the distribution of the O element is more dense, indicating the higher content of O in  $\text{CoFe}_2\text{O}_4$  and  $\text{CoMoO}_4$  than those of other elements. At the same time, combined with the illustrations in the EDS spectrum, it can be found that the atomic percentage contents of the Co, Fe and Mo elements in the  $\text{CoFe}_2\text{O}_4/\text{CoMoO}_4$  composite are 1 : 2 and 1 : 1, respectively, which further indicate

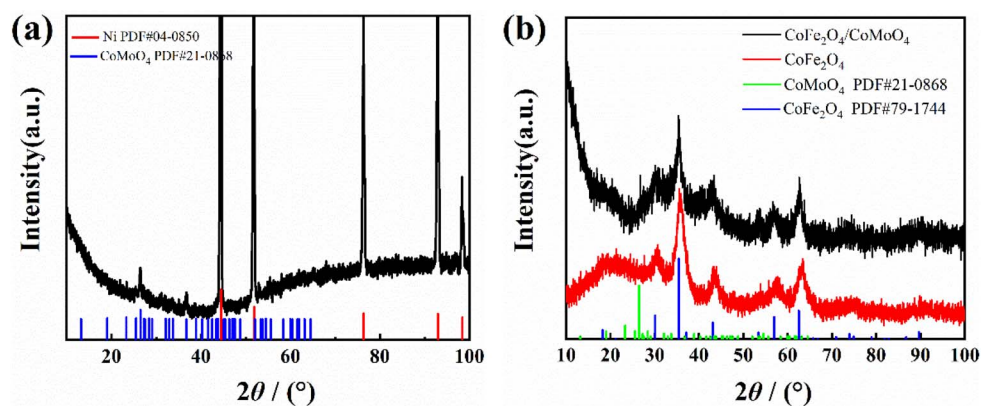


Fig. 3 XRD patterns of (a)  $\text{CoMoO}_4/\text{NF}$  and (b)  $\text{CoFe}_2\text{O}_4/\text{CoMoO}_4$ .

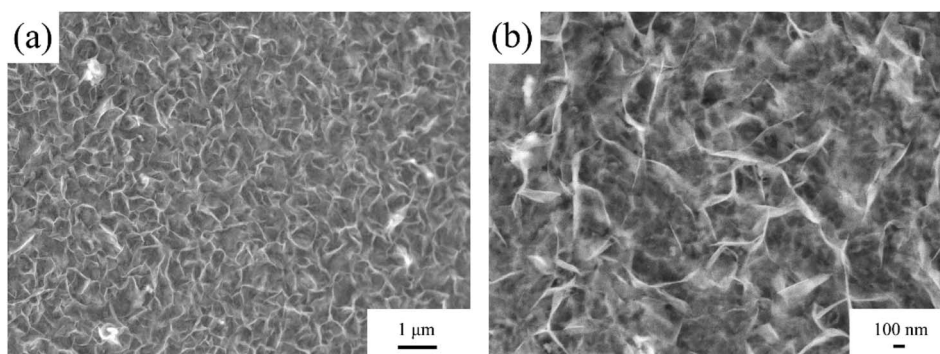


Fig. 4 SEM images of the  $\text{CoFe}_2\text{O}_4/\text{CoMoO}_4$  composite electrode material at different magnifications (a and b).



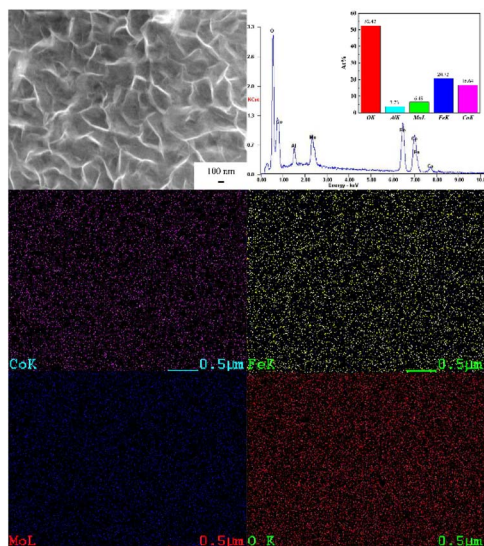


Fig. 5 Surface scan element distribution diagram of  $\text{CoFe}_2\text{O}_4/\text{CoMoO}_4$ .

that the composite material is reasonable in composition, uniform in distribution, and in line with the expected design. In addition, a small amount of Al (3.73 at.%) was detected, which is attributed to inadequate removal of  $\text{AlO}_2^-$  ions during washing, as well as the possibility of unreacted Al atoms remaining in the skeleton due to incomplete corrosion.

The microstructure of the two bimetallic oxides and the  $\text{CoFe}_2\text{O}_4/\text{CoMoO}_4$  composite electrode material is studied and characterized by TEM. The TEM image of  $\text{CoFe}_2\text{O}_4$  shown in Fig. 6(a) shows a rod-like skeleton structure distributed at multiple levels, while small holes distributed on the large skeleton structure can be seen, which is consistent with the structure shown by SEM. Fig. 6(b) shows the high-resolution transmission image of  $\text{CoFe}_2\text{O}_4$ . The crystal face spacings calculated by the analysis are 0.261 nm and 0.483 nm, corresponding to the (311) and (111) crystal faces of  $\text{CoFe}_2\text{O}_4$ . Fig. 6(c) shows the TEM image of the  $\text{CoFe}_2\text{O}_4/\text{CoMoO}_4$  composite, in which the sheet-like  $\text{CoMoO}_4$  is grown on the

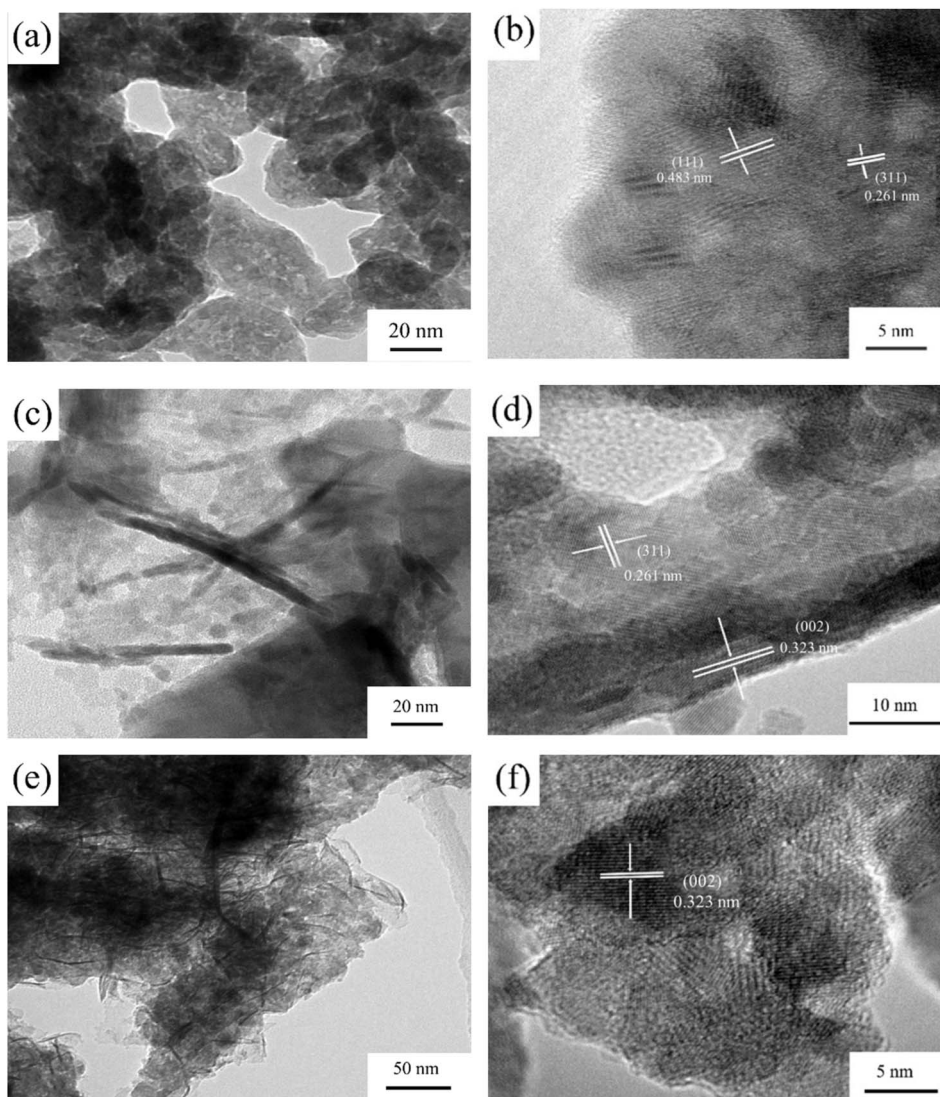


Fig. 6 TEM images of  $\text{CoFe}_2\text{O}_4$  (a and b),  $\text{CoFe}_2\text{O}_4/\text{CoMoO}_4$  (c and d) and  $\text{CoMoO}_4$  (e and f).



skeleton structure, and the distributed mesoporous structures can still be observed on the matrix skeleton of  $\text{CoFe}_2\text{O}_4$ , indicating that the skeleton structure of  $\text{CoFe}_2\text{O}_4$  is not affected or damaged after  $\text{CoMoO}_4$  is compounded. Lamellar  $\text{CoMoO}_4$  intergrowths will provide a more favorable reaction site for electrochemical reactions. Fig. 6(d) is the high-resolution transmission image of the  $\text{CoFe}_2\text{O}_4/\text{CoMoO}_4$  composite, in which mesoporous structures of about 10 nm exist on the skeleton structure, and ligament structures and lattice stripes are also observed on the skeleton. The measured lattice spacings of 0.261 nm and 0.323 nm correspond to the (311) plane of  $\text{CoFe}_2\text{O}_4$  and the (002) plane of  $\text{CoMoO}_4$  in the  $\text{CoFe}_2\text{O}_4/\text{CoMoO}_4$  composite, respectively. Fig. 6(e) shows the TEM image of  $\text{CoMoO}_4$ , in which abundant ligament structures are wrapped around the skeleton, agreeing well with the rich ligament structures shown in the SEM image. Fig. 6(f) shows its high-resolution transmission image, in which lattice streaks with different orientations can be observed on the lamellar structure with a hierarchical distribution. The crystal face spacing of 0.323 nm in the figure corresponds to the (002) crystal face of  $\text{CoMoO}_4$ . These TEM findings further confirm the composite structure indicated by XRD. Moreover, they offer a more direct view of the heterogeneous structure—a lamellar  $\text{CoMoO}_4$  phase supported by the  $\text{CoFe}_2\text{O}_4$  skeleton—compared to the SEM images.

The  $\text{CoFe}_2\text{O}_4/\text{CoMoO}_4$  composite was analyzed by X-ray photoelectron spectroscopy (XPS). Fig. 7(a) shows the high-resolution spectral fitting of the Co element. The peaks at the

binding energies of 780.95 eV and 796.59 eV correspond to the characteristic peaks of Co 2p, which belong to the Co  $2p_{3/2}$  and Co  $2p_{1/2}$  orbitals, respectively, indicating that Co exists in the +2 valence state.<sup>22</sup> At the same time, satellite peaks appeared at 784.01 eV, 787.11 eV, 790.35 eV, and 803.01 eV. Fig. 7(b) is the spectral diagram obtained by fitting the high-resolution spectrum of the Fe element. The peaks at 710.79 eV and 724.08 eV are assigned to  $\text{Fe}^{2+}$ , while those at 713.64 eV and 727.48 eV are assigned to  $\text{Fe}^{3+}$ . This shows that Fe exists in the +2 and +3 valence states,<sup>23,24</sup> while satellite peaks appear at 716.98 eV, 720 eV, and 732.85 eV. Fig. 7(c) is the spectrum obtained by fitting the high-resolution spectrum of Mo. The characteristic peaks corresponding to the energies of 232.44 eV and 235.56 eV belong to the Mo  $3d_{5/2}$  and Mo  $3d_{3/2}$  orbitals, respectively, with an energy difference of 3.12 eV. It is shown that Mo exists in the +6 valence state,<sup>25,26</sup> while satellite peaks appear at 233.73 eV and 236.52 eV. Fig. 7(d) is the spectrum obtained by fitting the high-resolution spectrum of O. The two peaks at the binding energies of 530.09 and 531.17 eV correspond to the characteristic peaks of O 1s, which is due to the interaction between Co–O, Fe–O and Mo–O in the sample of the  $\text{CoFe}_2\text{O}_4/\text{CoMoO}_4$  composite electrode material. At the same time, oxygen present due to the physical adsorption or chemisorption in the OH or C–O functional groups is reflected in it. To sum up, there are abundant valence states of Co, Fe and Mo in spinel  $\text{CoFe}_2\text{O}_4$  and scheelite  $\text{CoMoO}_4$ , which contribute to electron transfer during the hydrogen evolution and oxygen evolution reactions and enhance the conductivity of the material.

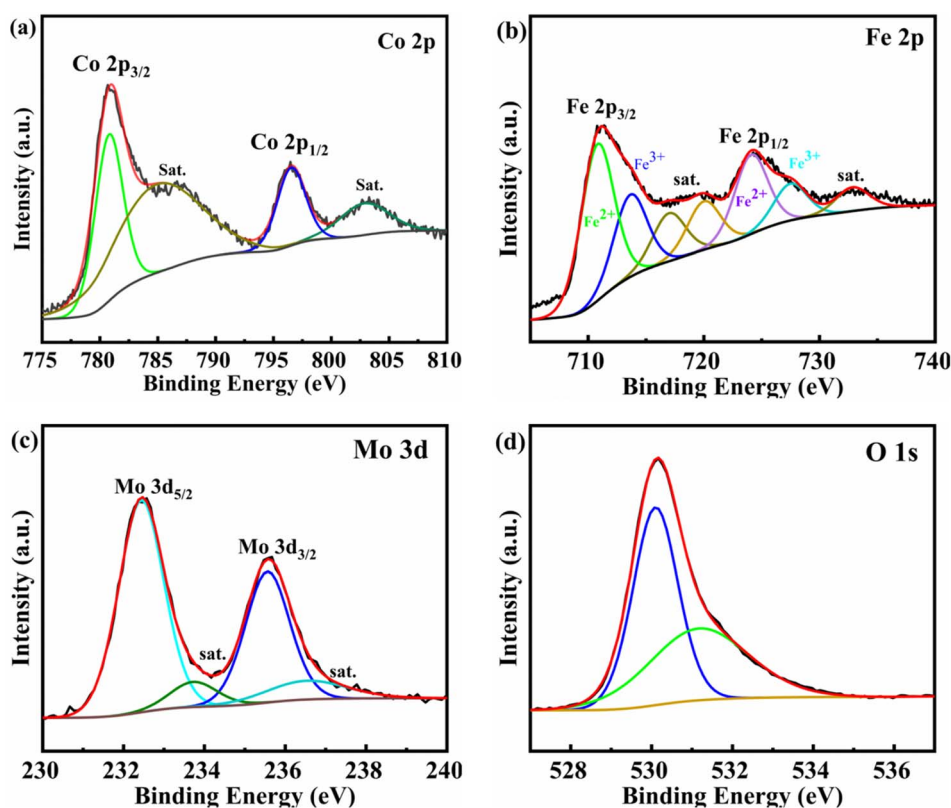


Fig. 7 XPS spectra of the  $\text{CoFe}_2\text{O}_4/\text{CoMoO}_4$  composite: (a) Co 2p; (b) Fe 2p; (c) Mo 3d; and (d) O 1s.



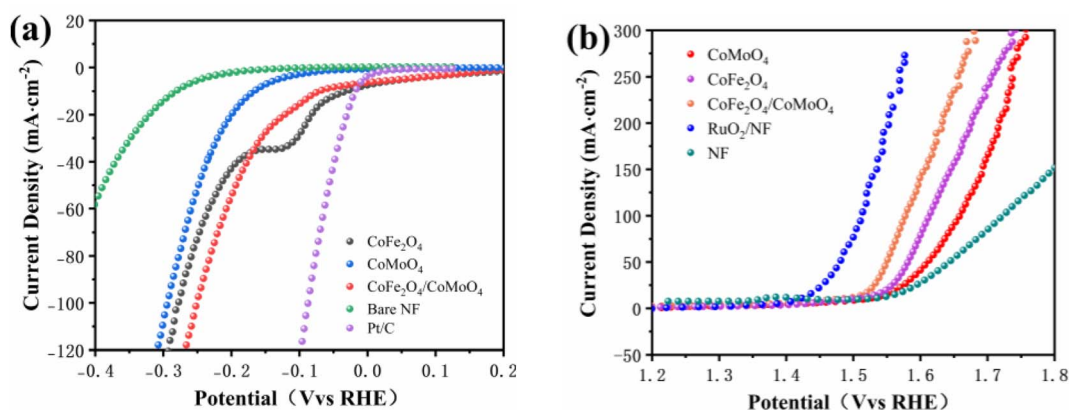


Fig. 8 Cathode polarization curves (a) and anode polarization curves (b) of each electrode material.

Table 1 Catalytic kinetic parameters of each electrode material

Electrode	b (mV <sup>-1</sup> dec <sup>1</sup> )		η@50 mA cm <sup>-2</sup> mV <sup>-1</sup>	
	HER	OER	HER	OER
CoMoO <sub>4</sub>	121.21	132.09	248	381
CoFe <sub>2</sub> O <sub>4</sub>	111.84	82.06	216	351
CoFe <sub>2</sub> O <sub>4</sub> /CoMoO <sub>4</sub>	100.44	70.47	193	319

Fig. 8(a) shows the cathode polarization curves of each electrode material. The overpotential of each electrode material at a current density of 50 mA cm<sup>-2</sup> is compared, as shown in

Table 1. As can be seen from the figure, CoFe<sub>2</sub>O<sub>4</sub>/CoMoO<sub>4</sub> has the best electrocatalytic hydrogen evolution activity, the lowest overpotential at the current density of 50 mA cm<sup>-2</sup>, and the best catalytic hydrogen evolution activity. Combined with its SEM and TEM results, it is clear that CoMoO<sub>4</sub> nanosheets grown on the CoFe<sub>2</sub>O<sub>4</sub> skeleton provide abundant active sites for the adsorption of H<sup>+</sup>. In addition, it is worth noting that CoFe<sub>2</sub>O<sub>4</sub> has an obvious reduction peak in the low overpotential region. Combined with the XPS analysis results, it can be seen that this is due to the inherent REDOX pairs of Co<sup>2+</sup>/Co<sup>3+</sup> and Fe<sup>2+</sup>/Fe<sup>3+</sup> in the spinel structure CoFe<sub>2</sub>O<sub>4</sub> and abundant valence state changes of CoMoO<sub>4</sub>. Therefore, the composite electrode

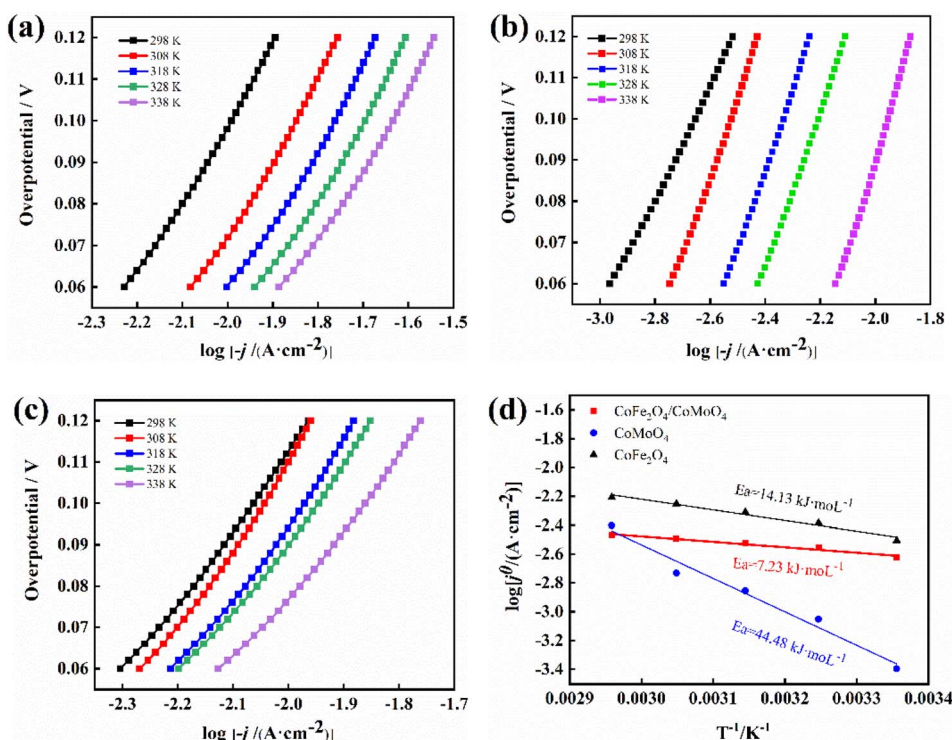


Fig. 9 Tafel curves of CoFe<sub>2</sub>O<sub>4</sub> (a), CoMoO<sub>4</sub> (b) and CoFe<sub>2</sub>O<sub>4</sub>/CoMoO<sub>4</sub> (c) at different temperatures and Arrhenius curve of each electrode material (d).



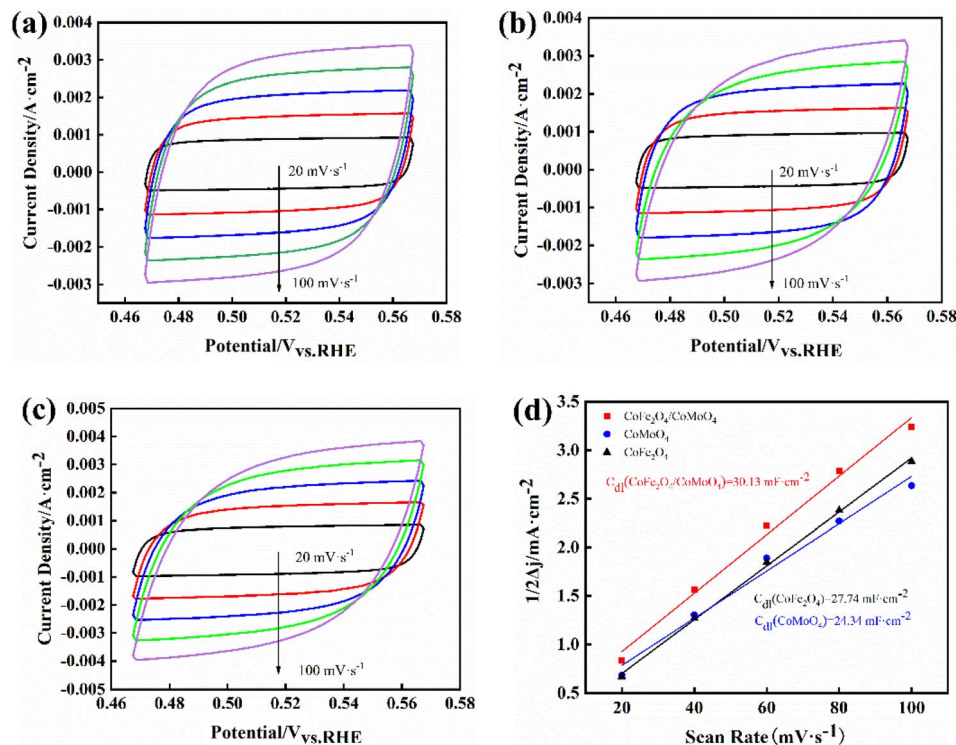


Fig. 10 CV curves of CoFe<sub>2</sub>O<sub>4</sub> (a), CoMoO<sub>4</sub> (b), and CoFe<sub>2</sub>O<sub>4</sub>/CoMoO<sub>4</sub> (c) at different scan rates. Relationship curve of  $\Delta j$  and scan rate of each electrode material (d).

material has a more favorable electron and ion transport process. At the same time, it can be seen from the Fig. 8(a) that the hydrogen evolution performance of CoMoO<sub>4</sub> is lower than that of CoFe<sub>2</sub>O<sub>4</sub>, which is mainly due to the unique structure of the small skeleton of CoFe<sub>2</sub>O<sub>4</sub> dependent on the large skeleton and the rich valence states of their respective elements. Furthermore, the skeleton structure of CoFe<sub>2</sub>O<sub>4</sub> after oxidation is rough and uneven, and there is a mesoporous structure of about 10 nm. Fig. 8(b) shows the anode polarization curves of electrocatalytic oxygen evolution of the above-mentioned electrode materials, and their overpotentials at a current density of 50 mA cm<sup>-2</sup> are compared. CoFe<sub>2</sub>O<sub>4</sub>/CoMoO<sub>4</sub> has the best electrocatalytic oxygen evolution activity and the lowest oxygen evolution overpotential at the current density of 50 mA cm<sup>-2</sup>. This shows that CoFe<sub>2</sub>O<sub>4</sub>/CoMoO<sub>4</sub> has the advantages of an excellent bifunctional catalyst. The hydrogen evolution properties and oxygen evolution properties of all electrode materials have the same catalytic properties, indicating that the oxide materials have similar properties in electrocatalytic hydrogen evolution and oxygen evolution.

Table 1 shows that CoFe<sub>2</sub>O<sub>4</sub>/CoMoO<sub>4</sub> has the lowest HER and OER Tafel slopes, with the HER slope of 100.44 mV dec<sup>-1</sup>, indicating that its hydrogen evolution process is controlled by the Volmer–Heyrovsky step,<sup>26</sup> which indicates that at low overpotentials, the CoFe<sub>2</sub>O<sub>4</sub>/CoMoO<sub>4</sub> composite electrode material can rapidly absorb/desorb H<sup>+</sup> and OH<sup>-</sup> ions in the electrolyte, thus breaking the dynamic balance between the oxidation and reduction reactions at the electrode/solution interface, and H<sup>+</sup> and OH<sup>-</sup> in the solution begin to accumulate on the electrode

surface. A sufficiently fast interfacial reaction rate is critical to effectively mitigate surface polarization. The lowest Tafel slope of the CoFe<sub>2</sub>O<sub>4</sub>/CoMoO<sub>4</sub> composite confirms its superior kinetics and thus the strongest depolarization ability during electrocatalysis. Fig. 9(d) shows the apparent activation energy of each electrode. The CoFe<sub>2</sub>O<sub>4</sub>/CoMoO<sub>4</sub> composite electrode has the lowest apparent activation energy of 7.23 kJ mol<sup>-1</sup>, indicating that it has the highest conversion efficiency and the fastest reaction speed in the catalytic reaction process.

In order to further study the electrochemically active surface area of CoFe<sub>2</sub>O<sub>4</sub>, CoMoO<sub>4</sub> and the CoFe<sub>2</sub>O<sub>4</sub>/CoMoO<sub>4</sub> composite electrode material participating in the reaction during electrocatalysis, the charging current in the potential window of the non-Faraday process was tested, obtaining a double-layer capacitance. Fig. 10(a)–(c) show the CV curves of the electrode materials at 0.47–0.57 V vs. RHE at scanning rates of 20, 40, 60, 80 and 100 mV s<sup>-1</sup>. It can be seen from the figure that the CV curves of the three electrodes all exhibit typical rectangular characteristics of double-layer capacitors. By calculating the current density difference  $\Delta j$  between the cathode and anode at 0.52 V vs. RHE, the double layer capacitance values of CoFe<sub>2</sub>O<sub>4</sub>,

Table 2 Surface parameters of each electrode material

Electrode	$C_d$ $\mu\text{F}^{-1}$	$S_r$ $\text{cm}^{-2}$	$r$
CoFe <sub>2</sub> O <sub>4</sub>	27 740	462	462
CoMoO <sub>4</sub>	24 340	406	406
CoFe <sub>2</sub> O <sub>4</sub> /CoMoO <sub>4</sub>	30 130	505	505



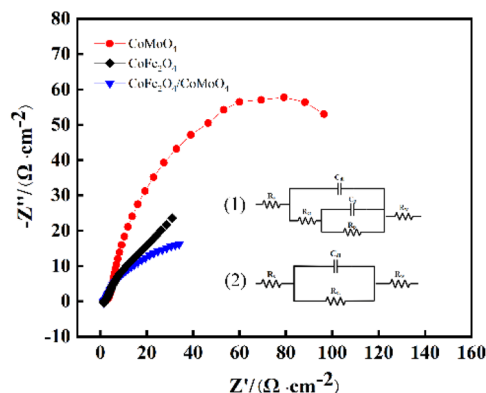


Fig. 11 Electrochemical impedance spectra and equivalent circuit diagrams of each electrode (inset). (1) CoMoO<sub>4</sub> and CoFe<sub>2</sub>O<sub>4</sub>/CoMoO<sub>4</sub> and (2) CoFe<sub>2</sub>O<sub>4</sub>.

CoMoO<sub>4</sub> and the CoFe<sub>2</sub>O<sub>4</sub>/CoMoO<sub>4</sub> composite electrode material are 27.74, 24.43 and 30.13 mF cm<sup>-2</sup>, respectively. The calculated surface parameters of each electrode are shown in Table 2. The CoFe<sub>2</sub>O<sub>4</sub>/CoMoO<sub>4</sub> composite electrode material has the largest electrochemical active surface area and roughness, indicating that it has the most exposed active sites.

To further probe the electrode reaction kinetics during the catalytic OER process, electrochemical impedance spectroscopy (EIS) measurements are performed within a frequency range of 10<sup>-2</sup> to 10<sup>5</sup> Hz, using an AC potential amplitude of 5 mV s<sup>-1</sup> (Fig. 11 and Table 3). For all samples, the tests were conducted at an overpotential of 100 mV. The comparable solution resistance ( $R_s$ ) confirms consistent electrolyte environments.<sup>27</sup> Nyquist plots reveal that the CoFe<sub>2</sub>O<sub>4</sub>/CoMoO<sub>4</sub> composite electrode material exhibits the lowest charge-transfer resistance ( $R_{ct} = 0.2657 \Omega$

cm<sup>-2</sup>), which was significantly lower than those of CoMoO<sub>4</sub> ( $R_{ct} = 0.8904 \Omega \text{ cm}^{-2}$ ) and CoFe<sub>2</sub>O<sub>4</sub> ( $R_{ct} = 6.919 \Omega \text{ cm}^{-2}$ ). This reduction indicates accelerated electron transfer across engineered interfaces, attributed to the synergistic effects of the CoFe<sub>2</sub>O<sub>4</sub>/CoMoO<sub>4</sub> heterojunction. Concurrently, the composite achieves the highest double-layer capacitance ( $C_{dl} = 0.4927 \mu\text{F}$ ), confirming an expanded electroactive surface area, while its minimal Warburg impedance ( $Y_0 = 0.06289 \text{ S sec}^{.5}$ ) demonstrates an optimized ion diffusion. Flaky CoMoO<sub>4</sub> nanosheets are vertically aligned on the CoFe<sub>2</sub>O<sub>4</sub> skeleton surface, providing abundant electrochemically active sites and maintaining efficient ion diffusion channels. Moreover, electronic structure modulation at the heterointerfaces reduces the energy barrier for electron transfer. Consequently, synergistic effects at the CoFe<sub>2</sub>O<sub>4</sub>/CoMoO<sub>4</sub> interface collectively enhance the OER activity.

The HER and OER together constitute electrolytic water reaction. Compared with the individual CoFe<sub>2</sub>O<sub>4</sub> and CoMoO<sub>4</sub>, the CoFe<sub>2</sub>O<sub>4</sub>/CoMoO<sub>4</sub> composite exhibited the best electrocatalytic performance for both HER and OER. Therefore, to evaluate its overall water-splitting performance, a two-electrode electrolyzer was constructed with the composite serving as both the anode and the cathode. The corresponding electrolytic curve is shown in Fig. 12(a). The electrolyzer achieved a low cell voltage of 1.55 V at a current density of 10 mA cm<sup>-2</sup>, demonstrating the excellent bifunctional electrocatalytic activity of the composite electrode. To preliminarily investigate the durability of the CoFe<sub>2</sub>O<sub>4</sub>/CoMoO<sub>4</sub> catalyst, a short-term stability test is performed at a constant current density of 30 mA cm<sup>-2</sup> for 12 hours, as shown in Fig. 12(b). The cell voltage increased by only 11 mV (0.6%) after continuous electrolysis, suggesting that the electrode maintains relatively stable performance under mild conditions. The porous skeleton obtained by dealloying and oxidation provides good support strength for the composite

Table 3 Fitting data of the equivalent circuit diagrams of different electrodes

Electrode	$R_s/\Omega \text{ cm}^{-2}$	$C_{dl}/\mu\text{F}$	$R_{ct}/\Omega \text{ cm}^{-2}$	$C_p/\text{F}$	$R_p/\Omega \text{ cm}^{-2}$	Warburg $Y_0/\text{S sec}^{.5}$
CoMoO <sub>4</sub>	1.622	0.1732	0.8904	0.07965	74.72	0.102
CoFe <sub>2</sub> O <sub>4</sub>	1.792	0.4309	6.919	—	—	0.1344
CoFe <sub>2</sub> O <sub>4</sub> /CoMoO <sub>4</sub>	1.619	0.4927	0.2657	0.142	8.563	0.06289

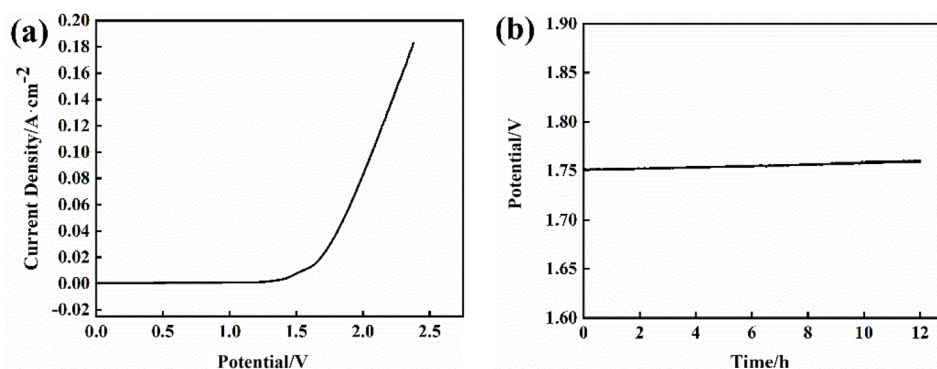


Fig. 12 Linear scanning curve (a) and stability (b) of the CoFe<sub>2</sub>O<sub>4</sub>/CoMoO<sub>4</sub> composite electrode material for the overall water splitting reaction.



material and further indicates the good bonding strength between the flaky CoMoO<sub>4</sub> and CoFe<sub>2</sub>O<sub>4</sub>.

## 4 Conclusion

In this study, a type of oxide composite material with different phase structures was synthesized by a hydrothermal method. CoFe<sub>2</sub>O<sub>4</sub> was used as the skeleton structure, and the sheet and fold structures of CoMoO<sub>4</sub> grew vertically on the surface of the CoFe<sub>2</sub>O<sub>4</sub> skeleton structure. This unique attachment structure was conducive to exposing more active sites. The structure offers abundant active sites and a extensive reaction interface, thereby facilitating highly efficient mass transport of H<sup>+</sup> and OH<sup>-</sup> ions as well as rapid charge transfer. In addition, the Co, Fe and Mo elements with abundant valence states provided favorable conditions for the transport of electrons and ions through abundant REDOX reactions in the electrocatalytic process, which helped to improve the electrocatalytic activity and reduce the reaction overpotential. Based on the unique structural advantages of spinel structure and scheelite structure and their synergistic effect, CoFe<sub>2</sub>O<sub>4</sub>/CoMoO<sub>4</sub> offered the best electrocatalytic activity. The skeleton structure obtained by dealloying combined with oxidation treatment exhibited a good structural stability and stable catalytic performance after long-term electrolysis.

## Conflicts of interest

There are no conflicts to declare.

## Data availability

The data that support the findings of this study are available within the article.

## Acknowledgements

The authors are grateful for the financial support from the National Natural Science Foundation of China (No. 51661018) and the National Natural Science Foundation of China (No. 22102066, No. 25JRRM004, and No. 25JRRM005).

## References

- 1 M. Chatenet, B. G. Pollet, D. R. Dekel, *et al.*, Water electrolysis: from textbook knowledge to the latest scientific strategies and industrial developments, *Chem. Soc. Rev.*, 2022, **51**, 4583–4762, DOI: [10.1039/D0CS01079K](https://doi.org/10.1039/D0CS01079K).
- 2 H. Sun, X. Xu, H. Kim, *et al.*, Electrochemical water splitting: Bridging the gaps between fundamental research and industrial applications, *Energy Environ. Mater.*, 2023, **6**, e12441, DOI: [10.1002/eem2.12441](https://doi.org/10.1002/eem2.12441).
- 3 M. I. Jamesh, D. Hu, J. Wang, *et al.*, Recent advances in noble metal-free electrocatalysts to achieve efficient alkaline water splitting, *J. Mater. Chem. A*, 2024, **50**, DOI: [10.1039/D3TA07418H](https://doi.org/10.1039/D3TA07418H).
- 4 Y. Zhang, C. G. Zhou, X. H. Yan, *et al.*, Recent advances and perspectives on graphene - based gels for superior flexible all - solid - state supercapacitors, *J. Power Sources*, 2023, **565**, 232916, DOI: [10.1016/j.jpowsour.2023.232916](https://doi.org/10.1016/j.jpowsour.2023.232916).
- 5 Y. Zhang, S. Hu, C. E. Li, *et al.*, Advanced strategies for enhancing electrochemical performance of NiAl LDH electrodes in supercapacitors, *Coord. Chem. Rev.*, 2025, **531**, 216497, DOI: [10.1016/j.ccr.2025.216497](https://doi.org/10.1016/j.ccr.2025.216497).
- 6 H. Liu, D. Ouyang, Q. Zhou, *et al.*, Successional heterostructure MoS<sub>2</sub>-Ni<sub>3</sub>S<sub>2</sub> nanospheres based on 3D nano-porous Ni: An efficient electrocatalyst for overall water splitting, *J. Alloys Compd.*, 2022, **920**, DOI: [10.1016/j.jallcom.2022.165243](https://doi.org/10.1016/j.jallcom.2022.165243).
- 7 D. Ouyang, H. Liu, Q. Zhou, *et al.*, Heterostructure MoS<sub>2</sub>/NiS supported on 3D nano-porous Ni as a highly efficient electrocatalyst for overall water splitting, *New J. Chem.*, 2025, **49**(8), 3119–3127, DOI: [10.1039/D4NJ04744C](https://doi.org/10.1039/D4NJ04744C).
- 8 D. Zhao, Z. Zhuang, X. Cao, *et al.*, Atomic site electrocatalysts for water splitting, oxygen reduction and selective oxidation, *Chem. Soc. Rev.*, 2020, **49**(7), 2215–2264, DOI: [10.1039/C9CS00869A](https://doi.org/10.1039/C9CS00869A).
- 9 X. Jian, M. Zhang, R. Li, *et al.*, Atomically dispersed ultralow-platinum loading on Ti<sub>3</sub>C<sub>2</sub>T<sub>x</sub> MXene as efficient catalyst for hydrogen evolution reaction, *Electrochim. Acta*, 2022, **411**, 411, DOI: [10.1016/j.electacta.2022.140091](https://doi.org/10.1016/j.electacta.2022.140091).
- 10 H. Chang, X. Li, L. Shi, *et al.*, Towards high-performance electrocatalysts and photocatalysts: Design and construction of MXenes-based nanocomposites for water splitting, *Chem. Eng. J.*, 2021, **421**, 129944, DOI: [10.1016/j.cej.2021.129944](https://doi.org/10.1016/j.cej.2021.129944).
- 11 X. Liu, H. Lu, S. Zhu, *et al.*, Alloying-Triggered Phase Engineering of NiFe System via Laser-Assisted Al Incorporation for Full Water Splitting, *Angew. Chem., Int. Ed.*, 2023, **62**(13), e202300800, DOI: [10.1002/anie.202300800](https://doi.org/10.1002/anie.202300800).
- 12 Y. Zhang, Y. F. Wei, X. Jing, *et al.*, One-step synthesis of nano-onion-like NiCoMn-LDHs for high-performance supercapacitors, *Int. J. Appl. Ceram. Technol.*, 2025, **22**(4), e15138, DOI: [10.1111/ijac.15138](https://doi.org/10.1111/ijac.15138).
- 13 X. Ren, Y. Zhai, Q. Zhou, *et al.*, Fabrication of nanoporous Ni and NiO via a dealloying strategy for water oxidation catalysis, *J. Energy Chem.*, 2020, **50**, DOI: [10.1016/j.jechem.2020.03.020](https://doi.org/10.1016/j.jechem.2020.03.020).
- 14 S. Liu, S. C. Lee, U. M. Patil, *et al.*, Controllable sulfuration engineered NiO nanosheets with enhanced capacitance for high rate supercapacitors, *J. Mater. Chem. A*, 2017, **5**, DOI: [10.1039/C6TA11049E](https://doi.org/10.1039/C6TA11049E).
- 15 T. Liu, P. Diao, Z. Lin, *et al.*, Sulfur and selenium doped nickel chalcogenides as efficient and stable electrocatalysts for hydrogen evolution reaction: The importance of the dopant atoms in and beneath the surface, *Nano Energy*, 2020, **74**, 11, DOI: [10.1016/j.nanoen.2020.104787](https://doi.org/10.1016/j.nanoen.2020.104787).
- 16 R. Mohili, N. R. Hemanth, H. Jin, *et al.*, Emerging high entropy metal sulphides and phosphides for electrochemical water splitting, *J. Mater. Chem. A*, 2023, **11**, 10463–10472, DOI: [10.1039/D2TA10081A](https://doi.org/10.1039/D2TA10081A).
- 17 W. Xu, G. Fan, S. Zhu, *et al.*, Electronic structure modulation of nanoporous cobalt phosphide by carbon doping for



- alkaline hydrogen evolution reaction, *Adv. Funct. Mater.*, 2021, **31**(48), 2107333, DOI: [10.1002/adfm.202107333](https://doi.org/10.1002/adfm.202107333).
- 18 T. Chen, M. Qian, X. Tong, *et al.*, Nanosheet self-assembled NiCoP microflowers as efficient bifunctional catalysts (HER and OER) in alkaline medium, *Int. J. Hydrogen Energy*, 2021, **46**(58), 29889–29895, DOI: [10.1016/j.ijhydene.2021.06.121](https://doi.org/10.1016/j.ijhydene.2021.06.121).
- 19 X. Du, J. Fu and X. Zhang, NiCo<sub>2</sub>O<sub>4</sub>@NiMoO<sub>4</sub> Supported on Nickel Foam for Electrocatalytic Water Splitting, *ChemCatChem*, 2018, **10**(23), 5533–5540, DOI: [10.1002/cctc.201801419](https://doi.org/10.1002/cctc.201801419).
- 20 Z. Zhang, X. Ma and J. Tang, Porous NiMoO<sub>4</sub>x/MoO<sub>2</sub> Hybrids as Highly Effective Electrocatalyst for Water Splitting Reaction, *J. Mater. Chem. A*, 2018, **6**, DOI: [10.1039/C8TA03047B](https://doi.org/10.1039/C8TA03047B).
- 21 D. Kim, X. Qin, B. Yan, *et al.*, Sprout-shaped Mo-doped CoP with maximized hydrophilicity and gas bubble release for high-performance water splitting catalyst, *Chem. Eng. J.*, 2021, **408**, 127331, DOI: [10.1016/j.cej.2020.127331](https://doi.org/10.1016/j.cej.2020.127331).
- 22 A. Samanta and C. R. Raj, A new approach for the synthesis of electrocatalytically active CoFe<sub>2</sub>O<sub>4</sub> catalyst for oxygen reduction reaction, *J. Electroanal. Chem.*, 2019, **847**(15), 113183, DOI: [10.1016/j.jelechem.2019.05.065](https://doi.org/10.1016/j.jelechem.2019.05.065).
- 23 R. Cheng, X. He, M. Jiang, *et al.*, f-p-d Gradient Orbital Coupling Induced Spin State Enhancement of Atomic Fe Sites for Efficient and Stable Oxygen Reduction Reaction, *Adv. Funct. Mater.*, 2025, 2425138, DOI: [10.1002/adfm.202425138](https://doi.org/10.1002/adfm.202425138).
- 24 R. Yang, X. Zheng, M. Qin, *et al.*, A Trifunctional Ni–P/Fe–P Collaborated Electrocatalyst Enables Self-Powered Energy Systems, *Advanced Science*, 2022, **9**(22), 2201594, DOI: [10.1002/advs.202201594](https://doi.org/10.1002/advs.202201594).
- 25 Y. N. Zhou, W. H. Hu, Y. N. Zhen, *et al.*, Metallic MoO<sub>x</sub> layer promoting high-valence Mo doping into CoP nanowires with ultrahigh activity for hydrogen evolution at 2000 mA cm<sup>-2</sup>, *Appl. Catal., B*, 2022, **309**, 121230, DOI: [10.1016/j.apcatb.2022.121230](https://doi.org/10.1016/j.apcatb.2022.121230).
- 26 C. T. Moi, A. Sahu and M. Qureshi, Tapping the potential of high-valent Mo and W metal centers for dynamic electronic structures in multimetallic FeVO(OH)/Ni(OH)<sub>2</sub> for ultrastable and efficient overall water splitting, *ACS Appl. Mater. Interfaces*, 2023, **15**(4), 5336–5344, DOI: [10.1021/acsami.2c21041](https://doi.org/10.1021/acsami.2c21041).
- 27 Y. Zhang, C. G. Zhou, X. H. Yan, *et al.*, Synthesis of Nafion-reduced graphene oxide/polyaniline as novel positive electrode additives for high performance lead-acid batteries, *Electrochim. Acta*, 2023, **466**, 143045, DOI: [10.1016/j.electacta.2023.143045](https://doi.org/10.1016/j.electacta.2023.143045).

